ISSN 1069-3513, Izvestiya, Physics of the Solid Earth, 2007, Vol. 43, No. 8, pp. 642–652. © Pleiades Publishing, Ltd., 2007.
Original Russian Text © M.Yu. Reshetnyak, 2007, published in Fizika Zemli, 2007, No. 8, pp. 24–34.

Thermal Convection and the Dynamo during Rapid Rotation

M. Yu. Reshetnyak

Schmidt Institute of Physics of the Earth, Russian Academy of Sciences,
Bol'shaya Gruzinskaya ul. 10, Moscow, 123995 Russia

Received December 5, 2006

Abstract—A dynamo model for an incompressible liquid in a rectangular rapidly rotating box is considered. The model is based on a pseudospectral method adapted for multiprocessor technology. The effect of rotation in Boussinesq models on some of the basic characteristics of flows is studied: the spatial form of fields, helicity generation, and spectra of fields. A mechanism stabilizing the magnetic field rise associated with the transition of the system to a nonlinear regime is analyzed separately. The results obtained in the paper provide deeper insights into the processes of magnetoconvection in the cores of planets.

PACS numbers: 91.25.Cw

DOI: 10.1134/S1069351307080046

1. INTRODUCTION

Conversion of thermal energy into the kinetic energy of motion of a conducting medium and further into the energy of a magnetic field is the subject of the dynamo theory [Zeldovich et al., 1983; Hollerbach and Rüdiger, 2004]. At present, the dynamo theory provides an explanation for magnetic fields observed in many astrophysical objects: the universe, galaxies and their clusters, stars, and planets.

In all these objects, the magnetic field exists for a considerably longer time than the characteristic time of dissipation, and this indicates the presence of a mechanism of field generation. Probably, the most remarkable results obtained in recent years in the field of the dynamo theory were derived from the modeling of geodynamo processes by Glatzmaier and Roberts [1995]. They considered the dynamo problem in the Earth's liquid core and developed a model in good agreement with both the observed magnetic field at the Earth's surface and some nonmagnetic benchmarks such as the rotational velocity of the Earth's solid core and (by the order of magnitude) the thermal, kinetic, and magnetic energy of fields. The unceasing interest in the works of Glatzmaier and Roberts is also due to the fact that their model is based on the concepts of small-scale fields, which have not been rigorously substantiated, so that the proposed models and hypotheses require interpretation and analysis. Since simple estimations (e.g., see [Reshetnyak, 2005]) show that the hydrodynamic and magnetic Reynolds numbers in the Earth's liquid core are large (Re ~ 10^9 and Re_m ~ 10^3), the description of the system behavior on small scales and the development of semiempirical models of turbulence are of fundamental importance for the geodynamo theory. In view of the fact that the cores of planets rotate rapidly, i.e., the daily rotation period is several orders of magnitude shorter than the characteristic convective times, inverse cascades of energies can arise [Lesieur, 1997; Tabeling, 2002]. This implies that, on small scales $l \ll \mathcal{L}$, where $\mathcal{L}$ is the scale of the core, not only the energy dissipation but also the energy flux to larger scales is possible. In the magnetic field problem, the magnetic energy can be transferred to larger scales due to nonlocal interactions, for example, from the scale of turbulence to the principal scale (the α effect), and locally across the spectrum, as is accepted in the Kolmogorov theory [Frisch, 1995]. It is obvious that the study of flow structure on small scales by means of direct numerical modeling is very important for the subsequent construction of large-scale dynamo models.

Although sphericity plays an important role in planetary dynamo problems, its incorporation only complicates the calculations involved in the modeling of small-scale fields. On the one hand, the Rossby scales $l_R \sim 10^{-5}\mathcal{L}$ (i.e., the scales on which the Coriolis force becomes of the same order as the nonlinear term in the Navier–Stokes equation) are still beyond the capabilities of the best modern computers; on the other hand, an increase in the density of grids in spherical coordinates leads to an excessive decrease in the time step. Modeling in Cartesian coordinates substantially extends the range of accessible scales and, because of the simpler form of equations in these coordinates, accelerates computations by at least one order of magnitude and improves the resolution. Thus, in planetary dynamo problems, it is possible that, on small scales $l \ll \mathcal{L}$, the field energy in the bulk of the liquid core is comparable to that on larger scales [Kutzner and Cristensen, 2002; Simitev, 2004] (see also the discussion in [Reshetnyak, 2006]). Since small-scale fields are invisible to the observer on the Earth's surface and their characteristics depend weakly on both the geometry of the region and

the boundary conditions [Sarson and Jones, 1997; Reshetnyak and Steffen, 2005], the analysis of the problem in a box can be very useful. Below, we examine how some interesting properties of a planetary dynamo system can be reproduced with the help of a sufficiently simple model in a rotating rectangular box simulating the behavior of magnetohydrodynamic turbulence far from solid boundaries.

2. DYNAMO EQUATIONS

We consider the dynamo equations for an incompressible liquid ($\nabla \cdot \mathbf{V} = 0$) in an infinite layer $0 \le z \le 1$ rotating at an angular velocity Ω about the vertical axis $\mathbf{z}$. We introduce the following units of measurement for the velocity $\mathbf{V}$, time t, pressure P, and magnetic field $\mathbf{B}$: κ/L, L^2/κ, $\rho\kappa^2/L^2$, and $2\Omega\rho\kappa\mu_0$, where L is the unit of length, κ is the coefficient of molecular thermal conductivity, ρ is the density of the material, and μ_0 is the magnetic constant. The system of dynamo equations in a Cartesian coordinate system (x, y, z) can then be written as (see the spherical geometry case in [Jones, 2000a])

$$\frac{\partial \mathbf{B}}{\partial t} = \mathrm{curl}(\mathbf{V} \times \mathbf{B}) + q^{-1}\Delta \mathbf{B},$$

$$\mathrm{EPr}^{-1}\left[\frac{\partial \mathbf{V}}{\partial t} - \mathbf{V} \times (\nabla \times \mathbf{V})\right] \tag{1}$$
$$= \mathrm{curl}\mathbf{B} \times \mathbf{B} - \nabla \mathbf{P} - \mathbf{1_z} \times \mathbf{V} + \mathrm{Ra}T\mathbf{1_z} + \mathrm{E}\Delta \mathbf{V},$$

$$\frac{\partial T}{\partial t} + (\mathbf{V} \cdot \nabla)(T + T_0) = \Delta T.$$

The dimensionless Prandtl, Ekman, Rayleigh, and Roberts numbers are $\mathrm{Pr} = \frac{\nu}{\kappa}$, $\mathrm{E} = \frac{\nu}{2\Omega L^2}$, $\mathrm{Ra} = \frac{\alpha g_0 \delta T L}{2\Omega\kappa}$, and $q = \frac{\kappa}{\eta}$, where ν is the kinematic viscosity, α is the volume expansion coefficient, g_0 is the gravitational acceleration, δT is the perturbation of the temperature T relative to the "diffuse" temperature distribution $T_0 = 1 - z$, and η is the magnetic diffusivity. We define the Rossby number as $\mathrm{Ro} = \mathrm{EPr}^{-1}$.

Since we are interested in small-scale solutions, we reduce, in the horizontal plane (x, y), the problem in an infinite layer to the problem in a box with boundary conditions periodic in x and y [Cattaneo, 2003]. At the boundaries $z = 0, 1$, we assume zero perturbations of temperature $T = 0$; considering the chosen profile of T_0, this is equivalent to the respective boundary temperatures $\mathcal{T} = T + T_0 = 1, 0$. For the velocity field, we assume the impenetrability condition and zero gradients of the tangential components of the field: $V_z = \frac{\partial V_x}{\partial z} = \frac{\partial V_y}{\partial z} = 0$ at $z = 0, 1$. We also require that the magnetic field normal component B_z at the boundary be continuous and the tangential field components vanish, $B_x = B_y = \frac{\partial B_z}{\partial z} = 0$. This formulation of the boundary conditions guarantees that the tangential components of the viscous stress tensor and the toroidal component of the magnetic field at the boundaries vanish.

3. NUMERICAL METHODS

3.1. Pseudospectral Method

The basic idea of the pseudospectral method is the numerical integration of equations in partial derivatives of form (1) in the wave space [Orszag, 1971]. In this case, the differentiation and integration operations reduce, respectively, to multiplication and division by the corresponding wave number, which ensures the computer accuracy of calculations. Nonlinear terms are calculated by transition to the physical space, multiplication of the fields, and backward transition to the wave space. In this approach, the majority of operations are performed to pass from one space to another and these transitions must be "fast." In the Cartesian coordinate system under consideration, we use the fast Fourier transform (FFT) adapted to parallel computations.

The system of equations (1) in the wave space can be written as [Buffett, 2003]

$$\left[\frac{\partial \mathbf{B}}{\partial t} + q^{-1}k^2\mathbf{B}\right]_\mathbf{k} = [\nabla \times (\mathbf{V} \times \mathbf{B})]_\mathbf{k},$$

$$\mathrm{E}\left[\mathrm{Pr}^{-1}\frac{\partial \mathbf{V}}{\partial t} + k^2\mathbf{V}\right]_\mathbf{k} = \mathbf{k}\mathcal{P}_k + \mathbf{F_k}, \tag{2}$$

$$\left[\frac{\partial T}{\partial t} + k^2 T\right]_\mathbf{k} = -[(\mathbf{V} \cdot \nabla)(T + T_0)]_\mathbf{k},$$

where

$$\mathcal{P}_\mathbf{k} = -\frac{\mathbf{k} \cdot \mathbf{F_k}}{k^2}, \quad k^2 = k_\beta k_\beta, \quad \beta = 1, \ldots, 3, \tag{3}$$

$$\mathbf{F_k} = [\mathrm{EPr}^{-1}\mathbf{V} \times (\nabla \times \mathbf{V}) + \mathrm{Ra}T - \mathbf{1_z} \times \mathbf{V} + (\mathbf{B} \cdot \nabla)\mathbf{B}]_\mathbf{k};$$

$\mathcal{T}$, $\mathbf{V}$, and $\mathbf{B}$ are 3-D Fourier transforms of the initial physical fields; and $\mathbf{k}$ is the wave vector. Let the field f in the physical space be specified on the grid $G = (1, \ldots, N_x; 1, \ldots, N_y; 1, \ldots, N_z)$. Then, the physical and wave representations in a box of height 1 with a square base of length λ are interrelated as

$$f(x, y, z) = \sum_{n_x = -N_x/2}^{N_x/2} \sum_{n_y = -N_y/2}^{N_y/2} \sum_{n_z = -N_z/2}^{N_z/2} \hat{f}(n_x, n_y, n_x) e^{i(k_x x + k_y y)} \phi(k_z z), \tag{4}$$

where

$$k_x = \frac{2\pi n_x}{\lambda}, \quad k_y = \frac{2\pi n_y}{\lambda}, \quad k_z = \frac{2\pi n_z}{\lambda}, \qquad (5)$$

and ϕ is sine or cosine (or their combinations), depending on the form of boundary conditions. Henceforth, for convenience, we omit the symbol $\hat{}$.

The Navier–Stokes equation in (2)–(5) requires an explanation. First, to reduce numerical instabilities due to aliasing, we wrote this equation in (1) in the conservative vorticity form [Canuto et al., 1988]. Furthermore, we excluded the pressure through the scalar multiplication of the equation of motion by $\mathbf{k}$ using the incompressibility condition $\mathbf{k} \cdot \mathbf{V} = 0$. We should note the following: (a) all fields are real and more efficient modifications of Fourier transforms can be used for the half-period, and (b) the fields have additional symmetry with respect to the z direction and can be expanded in sines or cosines, which further reduces the amount of calculations (for more detail, see [Press et al., 2002]). As additional boundary conditions in the k space, we set $T, \mathbf{V}, \mathbf{B} = 0$ for $\mathbf{k} = 0$.

For the integration over time, we used the explicit second-order Adams–Bashford (AB2) scheme for all terms except the diffusion term. To calculate the dissipative terms, we used the known "analytical" technique [Canuto et al., 1988]. We consider the equation

$$\frac{\partial A}{\partial t} + k^2 A = U. \qquad (6)$$

We rewrite it as

$$\frac{\partial A e^{k^2 \gamma t}}{\partial t} = U e^{k^2 \gamma t} \qquad (7)$$

and then apply the AB2 method to the new variables $\hat{A} = A e^{k^2 \gamma t}$ and $\hat{U} = U e^{k^2 \gamma t}$.

Below, we use the decomposition of solenoidal vector fields into the poloidal and toroidal components:

$$\mathbf{V} = \mathbf{V_P} + \mathbf{V_T}, \quad \mathbf{B} = \mathbf{B_P} + \mathbf{B_T}, \qquad (8)$$

where

$$\begin{aligned} \mathbf{V_P} &= \nabla \times \nabla \times (\mathbf{1}_z f), \quad \mathbf{V_T} = \nabla \times (\mathbf{1}_z e), \\ \mathbf{B_P} &= \nabla \times \nabla \times (\mathbf{1}_z h), \quad \mathbf{B_T} = \nabla \times (\mathbf{1}_z g), \end{aligned} \qquad (9)$$

and f, e, h, and g are scalar potentials depending on the radius vector $\mathbf{r}$ and time t. Then, we have in the wave space

$$\begin{aligned} e &= \frac{i(\mathbf{k} \times \mathbf{V})_z}{|k|^2}, \quad g = \frac{i(\mathbf{k} \times \mathbf{B})_z}{|k|^2}, \\ f &= \frac{V_z}{|k|^2}, \quad h = \frac{B_z}{|k|^2}. \end{aligned} \qquad (10)$$

On the strength of the orthogonality of the poloidal and toroidal components,

$$E_K = \frac{V^2}{2} = E_K^P + E_K^T, \quad E_M = \frac{B^2}{2\mathrm{Ro}} = E_M^P + E_M^T, \qquad (11)$$

it is convenient to introduce the energies related to the components:

$$E_K^P = \frac{V_P^2}{2}, \quad E_M^P = \frac{B_P^2}{2\mathrm{Ro}}, \quad E_K^T = \frac{V_T^2}{2}, \quad E_M^T = \frac{B_T^2}{2\mathrm{Ro}}. \qquad (12)$$

The Peclet, Reynolds, and magnetic Reynolds numbers are specified as

$$\mathrm{Pe} = \sqrt{2E_K}, \quad \mathrm{Re} = \mathrm{Pe}\,\mathrm{Pr}^{-1}, \quad R_m = \mathrm{Pe}q. \qquad (13)$$

We define the hydrodynamic helicity $\mathcal{H}^{\mathcal{H}}$ (for more detail, see [Reshetnyak, 2006]), current helicity $\mathcal{H}^{\mathcal{J}}$, magnetic helicity $\mathcal{H}^{\mathcal{M}}$, and cross-helicity $\mathcal{H}^{\mathcal{C}}$ [Brandenburg and Subramanian, 2005] as

$$\begin{aligned} \mathcal{H}^{\mathcal{H}} &= \langle \mathbf{V} \cdot \mathrm{curl}\mathbf{V} \rangle, \quad \mathcal{H}^{\mathcal{J}} = \mathrm{Ro}^{-1} \langle \mathbf{B} \cdot \mathrm{curl}\mathbf{B} \rangle, \\ \mathcal{H}^{\mathcal{M}} &= \mathrm{Ro}^{-1} \langle \mathbf{A} \cdot \mathbf{B} \rangle, \quad \mathcal{H}^{\mathcal{C}} = \mathrm{Ro}^{-1/2} \langle \mathbf{V} \cdot \mathrm{curl}\mathbf{B} \rangle, \end{aligned} \qquad (14)$$

where $\mathbf{A}$ is the vector potential ($\mathbf{B} = \nabla \times \mathbf{A}$). Taking into account the boundary conditions for $\mathbf{V}$ and $\mathbf{B}$, all helicities (14) vanish at the boundaries $z = 0, 1$. We also introduce the 3-D spectrum $F(k) = |f(k)|^2$ and the energy spectrum $E(k) = k^2 F(k)$.[1]

3.2. Parallelization and Tests

The next important step is to adapt the code to the multiprocessor technology. We used the presently most flexible MPI method, which allows calculations to be performed on computers of different architectures: both on computer clusters and on multiprocessor supercomputers with a common bus (in particular, IBM Regatta p69+ supercomputers). The essence of parallelization is that the wave and physical spaces are partitioned between the processors in one or more directions, so that the further computations are performed on each processor independently, with periodic data exchange

[1] In a strict sense, the coefficient k^2 is valid for a homogeneous isotropic field.

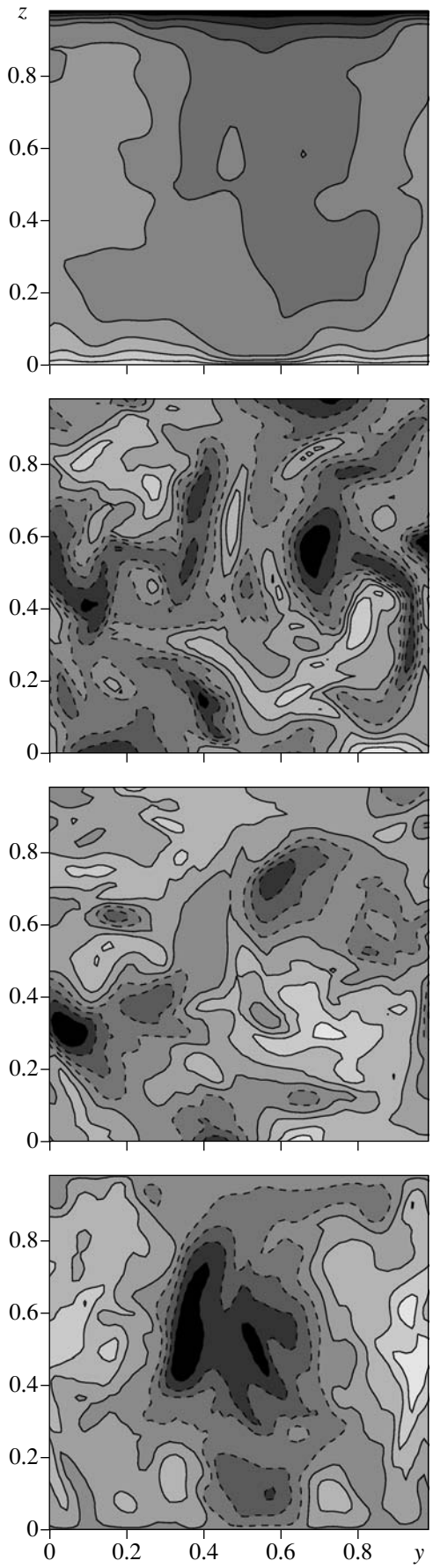

Fig. 1. No-rotation regime, $\mathbf{B} = 0$, with the grid $N = N_x = N_y = N_z = 64$. Characteristic distributions of the fields (from top to bottom) $T + T_0$, V_x, V_y, and V_z for $E = 10^{-6}$, $Pr = 0.1$, and $Ra = 1.5$. The respective field ranges are (0, 1), (–123, 146), (–184, 150), and (–257, 231). Darker areas bounded by broken lines correspond to negative values of fields.

between the processors. Since we used computers with a relatively small number of processors (a few tens), we chose 1-D partitioning in the z direction for the k space and in the y direction for the configuration space (details on the 2-D partitioning adjusted to Cray computers can be found in [Cattaneo et al., 2003]). A nontrivial problem is the adaptation of a 3-D fast transform that is a sequence of three 1-D FFTs. There are two strategies: (i) to perform two 1-D FFTs (without data exchange between the processors) and one multiprocessor FFT (with data exchange) or (ii) to use two 1-D FFTs (i.e., to perform a 2-D transform in x, y) without data exchange; transpose the matrices, e.g., in planes $y = \text{const}$, with data exchanged between the processors; and then perform the final FFT in the z direction. In this case, the FFT itself does not require data exchange. In this work, we used the second strategy. An additional processor was assigned for the synchronization of collective operations and input–output operations.

The algorithm described above was written in FORTRAN-95 and has been tested on numerous analytical examples. The following general approach was applied in these tests. We considered an arbitrary parabolic equation of the form

$$\frac{\partial \mathbf{G}}{\partial t} = \hat{\mathbf{H}}(\mathbf{X}), \tag{15}$$

where $\hat{\mathbf{H}}$ is a known differential operator and $\mathbf{X}$ is a vector, $\mathbf{X} = (T, \mathbf{V}, \mathbf{B})$. Let $\mathbf{X}_0 = \mathbf{X}(t_0)$. The value $\mathbf{h} = \hat{\mathbf{H}}(\mathbf{X}_0(x, y, z))$ is then calculated analytically and the source $\mathbf{g} = -\mathbf{h}$ is added to the right-hand side of (15). Integrating the resulting equation numerically, we should make sure that $\frac{\partial \mathbf{G}}{\partial t} = 0$ for an arbitrary initial value $\mathbf{X}_0$ satisfying the formulation of the problem. Note that, for such tests, it is convenient to use symbolic algebra packages (for example, Maple or Mathematica) that can convert analytical expressions obtained for $\mathbf{g}$ into FORTRAN or C codes. This approach greatly facilitates the search for errors, allowing one to find points in space at which the divergence from the analytical solution is greater than the accuracy defined by the time integration scheme.

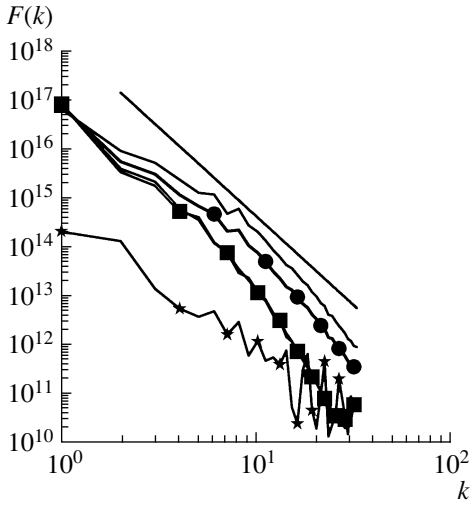

Fig. 2. No-rotation regime. The 3-D spectrum of the temperature field fluctuation 10^7T^2 is shown by stars, the kinetic energy spectra $f_x = F_K(k_x, k_y = k_z = 1)$ and $f_y = F_K(k_y, k_x = k_z = 1)$ are shown by squares, the kinetic energy spectrum $f_z = F_K(k_x = k_y = 1, k_z)$ is shown by a solid line, and the averaged kinetic energy spectrum $F(k) = (f_x + f_y + f_z)/3$ is shown by solid circles. The linear plot is the Kolmogorov spectrum $F(k) \sim k^{-11/3}(E_K(k) \sim k^{-5/3})$.

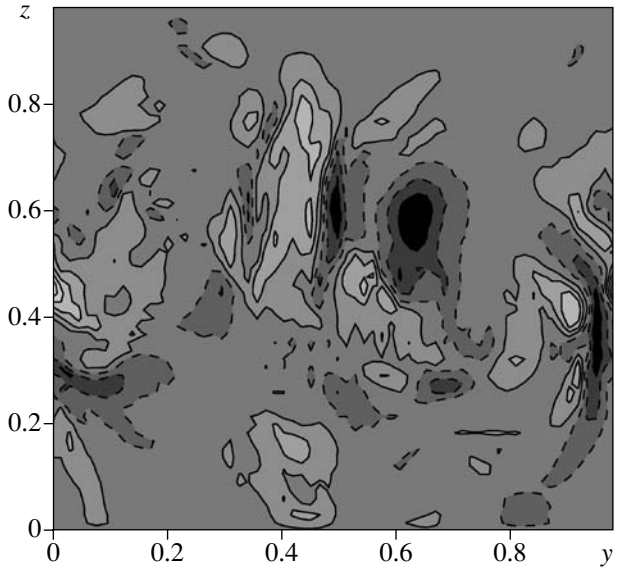

Fig. 3. Distribution of the hydrodynamic helicity $\mathcal{H}^{\mathcal{H}}$ covering the range $(-9 \times 10^5, 2 \times 10^6)$.

4. MODELING RESULTS

4.1. Thermal Convection without a Magnetic Field: No-Rotation Case

The regime without rotation, both without a magnetic field (see the review in [Getling, 1999]) and in the complete dynamo problem (see references in [Jones and Roberts, 2000b; Cattaneo et al., 2003; Brandenburg and Subramanian, 2005]), has been the subject of numerous studies, and we focus only on some important aspects. The onset of convection in an infinite plane layer is a threshold phenomenon resulting from an increase in the Rayleigh number to the critical value $\mathrm{Ra}^{\mathrm{cr}}$ with $n_x = n_y = \pi/\sqrt{2}$, $n_z = 1$ [Chandrasekhar, 1961]. Figure 1 presents cross sections of fields for the developed thermal convection mode with $\mathrm{Re} \sim 5 \times 10^3$ s and with quasi-periodic behavior of the energy with time $E_K(t)$. The field spectra are close to the Kolmogorov dependence (Fig. 2). The observed weak anisotropy of the kinetic energy spectra is due to the presence of the preferred z direction of the gravitational force.

It is noteworthy that the arising small-scale hydrodynamic helicity $\mathcal{H}^{\mathcal{H}}$ (Fig. 3) has a distribution close to that observed in [Meneguzzi and Pouquet, 1989]. Since no preferred direction exists in the case without rotation, the volume-averaged helicity $\overline{\mathcal{H}^{\mathcal{H}}_{\mathrm{v}}}$ is zero (for details of the mean-field dynamo theory, see [Moffat, 1978; Krause and Rädler, 1980; Zeldovich et al., 1983]).

4.2. Thermal Convection with Rotation

The regime with rotation ($\mathrm{E} \ll 1$) is typical of convection in the cores of planets.[2] Small values of Ra can result in horizontal rolls rotating about the vertical axis; however, with an increase in Ra, the role of these modes becomes insignificant (for more detail, see [Jones and Roberts, 2000b]), while cyclonic modes elongated along the rotational axis z and having the diameter $l_c \sim \mathrm{E}^{1/3}$ become more significant [Chandrasekhar, 1961; Roberts, 1965; Busse, 1970]. The appearance of a small scale in the horizontal direction leads to an increase in $\mathrm{Ra}^{\mathrm{cr}} \sim \mathrm{E}^{-1/3}$. Figure 4 shows the characteristic field distributions for a well-expressed geostrophic flow with a dense distribution of cyclones and anticyclones. Relatively small oscillations of the kinetic energy are observed along with synchronous variations in the poloidal and toroidal components ($E_K^T \gtrsim E_K^P$).

Now we examine more closely variations in spectra due to an increase in Ra (Fig. 5). For small $\mathrm{Ra} \sim \mathrm{Ra}^{\mathrm{cr}}$, the kinetic energy spectrum displays a well-pronounced peak at $k \sim k_c$ close to that predicted by the linear theory. The spectrum rapidly decreases at $k > k_c$. An increase in Ra causes the spectrum to be filled in the region $k_c < \mathrm{E}^{-1/3}$ ($k_c \sim 1/l_c$), so that the spectral amplitude at small k becomes comparable with or even higher than the amplitude at k_c. Since the Earth's liquid core values are $\mathrm{E} \sim 10^{-15}$ and $l_c \sim 10^{-5}\mathcal{L}$ and only the first ten harmonics at the surface of the core are known from magnetic field observations, prediction of the

[2] $\mathrm{E} \sim 10^{-15}$ for the Earth's liquid core.

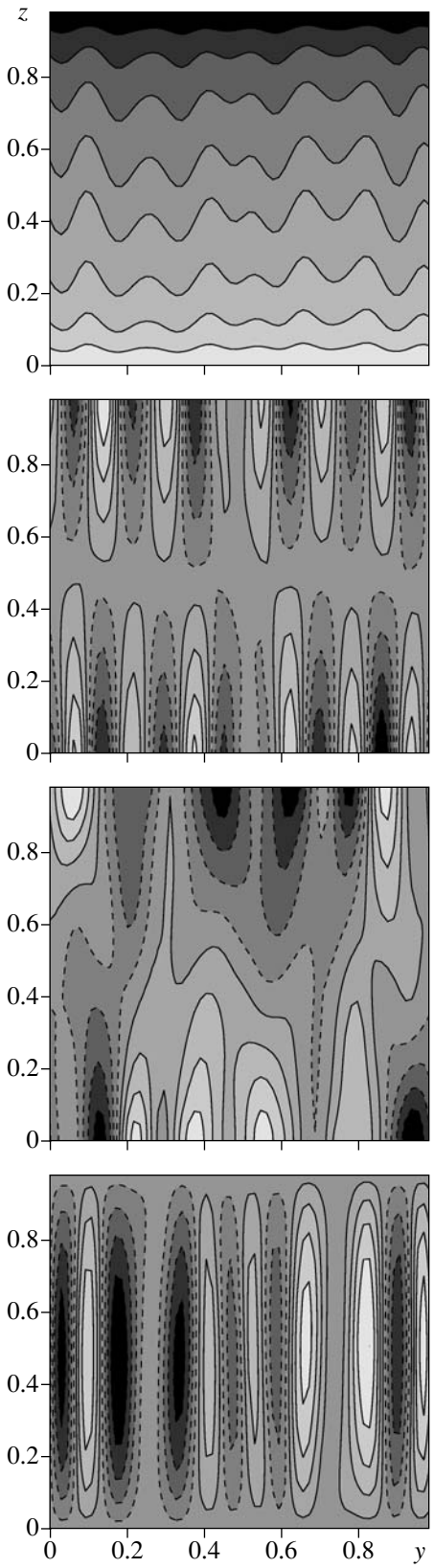

Fig. 4. Regime with rotation (**B** = 0). The characteristic distributions of the fields (from top to bottom) $T + T_0$, V_x, V_y, and V_z for $E = 3 \times 10^{-5}$, Pr = 1, and $Ra = 4 \times 10^2$. The respective field ranges are (0, 1), (–196, 196), (–94, 94), and (–152, 152).

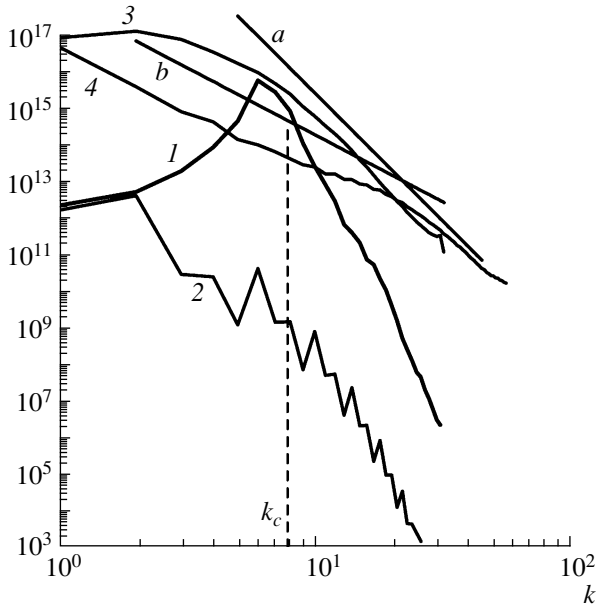

Fig. 5. Convection with rotation (**B** = 0). Kinetic energy spectra $f_x = F_K(k_x, k_y = k_z = 1)$ and $f_y = F_K(k_y, k_x = k_z = 1)$ (curve *1*) and $f_z = F_K(k_x = k_y = 1, k_z)$ (curve *2*) calculated for $E = 3 \times 10^{-5}$, Pr = 1, and $Ra = 4 \times 10^2$; the respective spectra for $Ra = 1.2 \times 10^3$ are plotted as curves *3* and *4*. Linear dependences *a* and *b* correspond to $F(k) \sim k^{-7}$ and $F(k) \sim k^{-11/3}$. The vertical dashed line $k_c \sim E^{-1/3}$ shows the position of the principal cyclonic mode predicted by the linear theory.

spectrum behavior in the range $l < 0.1\mathcal{L}$ is of great importance for the general theory. The resulting pattern is close to that inferred from calculations of the 3-D problem of thermal convection in a sphere [Reshetnyak, 2006]; however, the scalings at $k > k_c$ are different for different geometries and most probably depend on concrete parameters (for example, on the value of Ra).

Note that the spectra depend on direction (anisotropy), which is the basic distinction from the no-rotation case: in both cases presented in Fig. 5, the kinetic energy spectra in the vertical direction decrease exponentially, whereas the spectra in the horizontal plane have a maximum or a kink related to cyclonic structures and shifting toward larger scales with an increase in Ra.

The system of cyclones and anticyclones has a large-scale hydrodynamic helicity $\mathcal{H}^{\mathcal{H}}$ such that $\mathcal{H}^{\mathcal{H}}(z) > 0$ at $0 < z < 0.5$ and $\mathcal{H}^{\mathcal{H}}(z) < 0$ at $0.5 < z < 1$. These relations express the law of conservation of angular momentum for a cyclone or an anticyclone. Most correlated are strongly geostrophic flows with small Reynolds numbers Re (Fig. 6). An increase in Ra leads to an effective decrease in $\mathcal{H}^{\mathcal{H}}$. Evidently, at fixed E, an increase in Ra would lead to an initial Kolmogorov pattern with a relatively low value of $\mathcal{H}^{\mathcal{H}}$ because

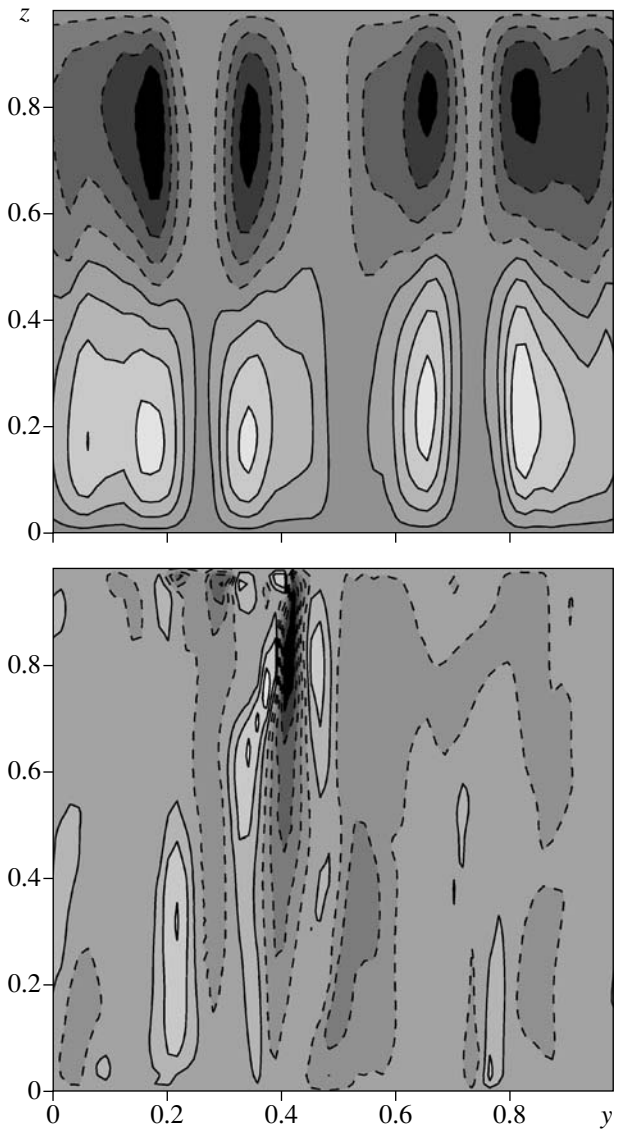

Fig. 6. Distribution of the hydrodynamic helicity $\mathcal{H}^{\mathcal{H}}$ for Ra = 4×10^2 (upper panel, the range from -7×10^5 to 7×10^5) and for Ra = 1.2×10^3 (lower panel, the range from -2.3×10^7 to 2.3×10^7).

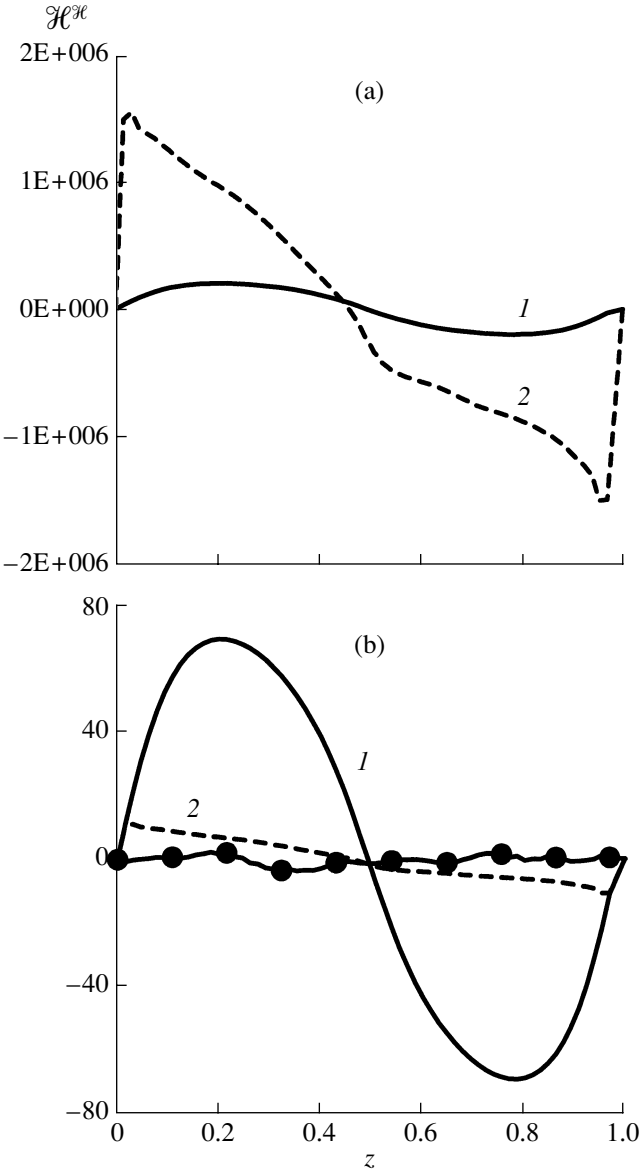

Fig. 7. Upper panel: the hydrodynamic helicity profile $\mathcal{H}^{\mathcal{H}}(z)$ for E = 3×10^{-5}, Pr = 1, Ra = 4×10^2 (solid curve) and Ra = 1.2×10^3 (dashed curve). Lower panel: the respective values normalized to the volume-averaged kinetic energy $\overline{E_K}$. The curve with circles is calculated for the no-rotation case.

of the weak correlation between the velocity **V** and the vorticity $\omega = \nabla \times \mathbf{V}$. This decrease in correlation is clearly observed in Fig. 7, where the helicity values are normalized to the kinetic energy. It is also noteworthy that, with increasing Re, the helicity tends to concentrate at the solid boundary and, by virtue of the specific boundary conditions, an $\mathcal{H}^{\mathcal{H}}$ boundary layer arises at $z = 0, 1$. With the exception of regions near the boundaries, where $\mathcal{H}^{\mathcal{H}}|_{z=0,1} = 0$, the dependence $\mathcal{H}^{\mathcal{H}}(z) = C_H(0.5 - z)$, where C_H is a constant coefficient, can be assumed at large values of Re that are, however, still consistent with the geostrophic approximation. Note that, as seen from Fig. 7, the coordinates λ_1 and λ_2 of the maximums of $|\mathcal{H}^{\mathcal{H}}|$ for the regimes with $\mathrm{Re}_1 = 260$ and $\mathrm{Re}_2 = 1960$ are evidence for an inverse dependence: $\lambda_1/\lambda_2 \sim \mathrm{Re}_2/\mathrm{Re}_1 \approx 7$. Recall that the boundary layer theory [Schlichting, 1968] implies that $V_x \sim V_y \sim \mathrm{Re}$, $V_z \sim \mathrm{Re}^{1/2}$, and $\delta_z \sim \mathrm{Re}^{-1/2}\mathcal{L}$ near a boundary. The latter relation is, generally speaking, consistent with our estimate because, with an approach to the wall, the decrease in V_z is accompanied by an increase in ω_z. We obtained the following upper-bound estimate for the helicity amplitude: $C_H \sim V_z\omega_z \sim \mathrm{Re}^{1/2}\mathrm{Re}\,\mathrm{E}^{-1/3} = \mathrm{Re}^{3/2}\mathrm{E}^{-1/3}$. The calculations demonstrate a weaker dependence on Re: $C_H \sim$

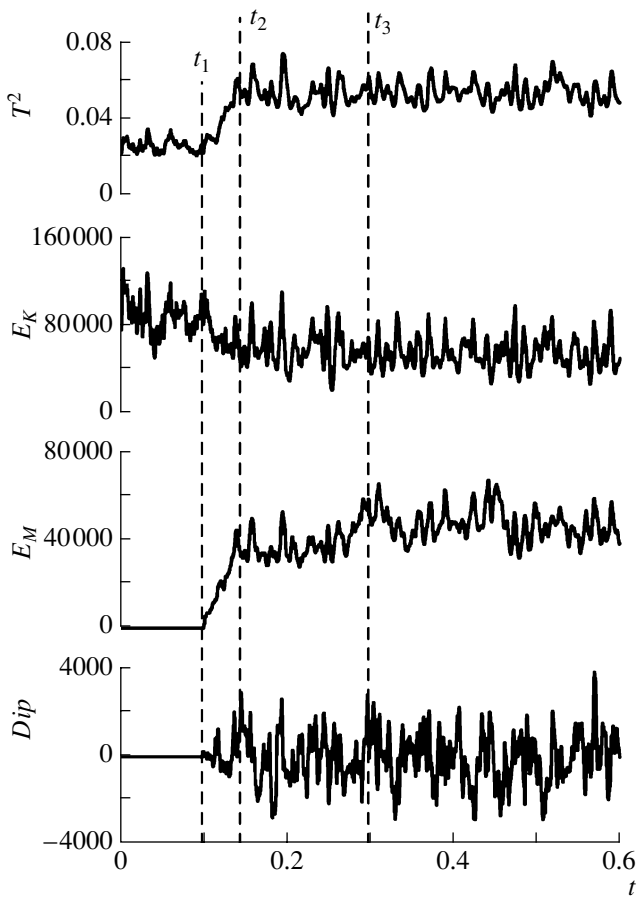

Fig. 8. Temporal evolution of the following volume-integrated values (from top to bottom): squared fluctuation of the temperature T^2, kinetic energy E_K, magnetic energy E_M, and vertical magnetic dipole *Dip*; the curves were calculated on the grid $N = N_x = N_y = N_z = 32$ for $E = 10^{-4}$, Pr = 1, Ra = 6×10^2, and $q = 10$. An incipient magnetic field arises at the time t_1. The time t_3 marks the onset of the steady-state regime, when the magnetic energy stops increasing.

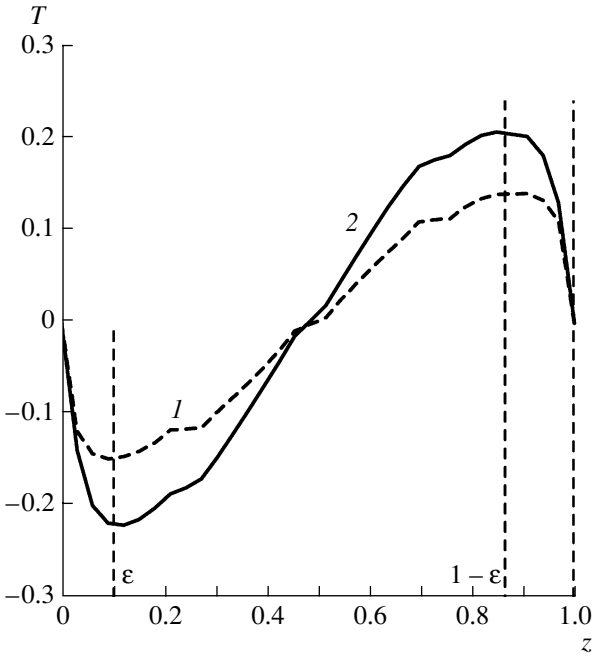

Fig. 9. Vertical temperature perturbation profile for the regimes shown in Fig. 8: (*1*) without a magnetic field, $t < t_1$; (*2*) with a magnetic field, for $t > t_3$. The temperature jump in the boundary layer of the thickness ε increases in the presence of the magnetic field.

Re. We are inclined to attribute this difference to a decrease in the correlation between **V** and ω. The helicity of different signs generated near the boundaries is transported by vertical flows into the bulk volume.

4.3. Dynamo

The problem with a magnetic field qualitatively differs from the convection problem first of all because it has a different set of conservation laws. For example, in the inviscid approximation, the Navier–Stokes equation for a 3-D case has two integrals of motion: the kinetic energy E_K and the hydrodynamic helicity $\mathcal{H}^{\mathcal{H}}$. For the problem with a magnetic field in the absence of external forces and dissipation, the conservation law is valid for the sum of the kinetic and magnetic energies, as is the law of conservation of the magnetic helicity $\mathcal{H}^{\mathcal{M}}$ and the cross-helicity $\mathcal{H}^{\mathcal{C}}$ (14). It can be shown (e.g., see [Brandenburg and Subramanian, 2005]) that this difference leads to far-reaching consequences and can result in additional inverse energy cascades across the spectrum. Further, we examine the response of the system of flows considered above to the application of a weak incipient magnetic field and its increase and the transition of the system to the saturation regime.

As is known (e.g., see [Moffatt, 1978]), magnetic field generation is a threshold phenomenon and begins when the magnetic Reynolds number reaches a certain critical value. If a backward effect of the magnetic field on the flow is absent, the magnetic energy exponentially increases or decreases, depending on the level of supercriticality. This regime is called the kinematic dynamo (KD) regime. Figure 8 shows the transition of the system from a state of thermal convection without a magnetic field ($0 < t < t_1$) to the KD regime ($t_1 < t < t_2$) and further to a nonlinear regime with high magnetic energies ($t > t_2$). Note the abrupt increase in the squared fluctuation of the temperature T^2 during the transition $1 \longrightarrow 2$. Figure 9 shows $T(z)$ profiles with well-defined boundary layers of a thickness ε. In spite of the overall decrease in the energy of vertical convective motions $\sim V_z^2/2$ due to a magnetic field, the jump in the layer becomes greater (for more detail, see the analysis of the Gartmann layer in [Landau and Lifshitz, 1982]).

Now we consider in greater detail the evolution of energies with time. We have $E_K^1 = (8.7 \pm 1.5) \times 10^4$ in

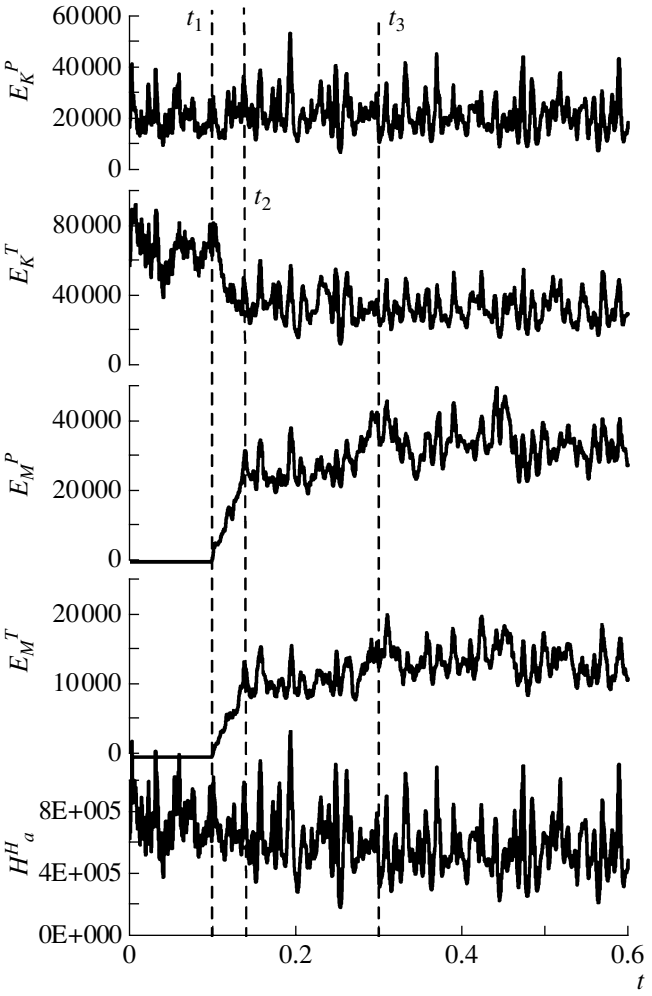

Fig. 10. Evolution of the volume-integrated poloidal (E_K^P) and toroidal (E_K^T) kinetic energies, poloidal (E_M^P) and toroidal (E_M^T) magnetic energies, and intensity of the hydrodynamic helicity $\mathcal{H}_a^{\mathcal{H}}$.

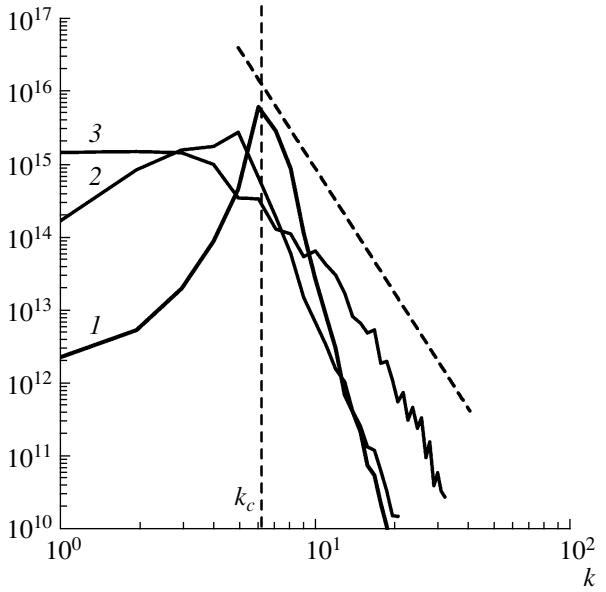

Fig. 11. Convection with rotation and a magnetic field calculated on the grid $N = N_x = N_y = N_z = 64$ for $E = 3 \times 10^{-5}$, Pr = 1, $Ra = 4 \times 10^2$, and $q = 3$: (*1, 2*) spectra of the kinetic energy (*1*) F_K ($B = 0$, $t < t_1$) and (*2*) F_K ($B \neq 0$, $t > t_3$); (*3*) spectrum of the magnetic energy F_M for $t > t_3$. The inclined dashed line plots the relation $F(k) \sim k^{-5.5}$.

the range $0 < t < t_1$. As the magnetic field further increases, the kinetic energy decreases by a factor of 0.6: $E_K^1 = (5.5 \pm 1.4) \times 10^4$. In the saturation regime, $E_K/E_M \sim 1.2$ and the oscillation amplitude is small: $E_M = (4.6 \pm 0.8) \times 10^4$. The phase 2 ⟶ 3 is unrelated to a change in the large-scale component of the magnetic field. This is indirectly supported by the stationary amplitude of oscillations of the reversing magnetic dipole $Dip = \mathrm{Re}B_z$ corresponding to the harmonic with $k = (1, 1, 1)$ against the background of an overall increase in E_M (Fig. 8). During the transition 1 ⟶ 3, the total energy of the system $E = E_K + E_M$ remains constant.

However, on the basis of the above analysis, it is premature to conclude that the influence of the magnetic field on the flow reduces only to a decrease in the magnetic Reynolds number and, as a consequence, the termination of generation. This influence is found to be selective and substantially different for different components of the velocity field. This inference explicitly follows from the evolution of the toroidal and the poloidal kinetic energy (Fig. 10). The observed decrease in the total kinetic energy is due only to a change in the toroidal (tangential) component (by a factor of 1.9), with the poloidal (vertical) component being constant. In other words, the magnetic field prevents the development of small-scale cyclonic rotation. The temporal evolution of E_M^P and E_M^T is morphologically similar. The ratio of their averages for $t > t_3$ is $\overline{E_M^P}/\overline{E_M^T} = 2.5$.

Analysis of the curves of $E_K(t)$ and $E_M(t)$ shows that, at the kinematic stage, some peaks correlate, whereas, with an increase in E_M, magnetic energy peaks start to lag behind the corresponding E_K peaks by one-fourth of the period. An increase in the magnetic field suppresses the rise in the kinetic energy, and the total energy of the system begins to decrease. It is possible that the backward effect of the magnetic field on the system arises only if a certain critical value is reached, for example, if the sum of the fluctuating and mean fields exceeds a threshold value, as is the case with the Sun [Ruzmaikin, 2001].

In addition to the selective suppression of velocity field components, differential scale-dependent suppres-

sion of convection takes place. Figure 11 presents energy spectra of a higher resolution for two typical regimes without and with a magnetic field that were examined above. The application of the magnetic field leads to a stronger decrease in the amplitude of large-scale modes of the velocity field, thereby suppressing the rise in the magnetic field. On the other hand, the kinetic energy spectrum remains constant for $k > (2$ to $3)k_c$, suggesting that the magnetic field on these scales is force-free. Note that, at high k, the magnetic energy is substantially greater than the kinetic energy. It is also interesting that the maximum in the kinetic energy spectrum is more pronounced than in the magnetic energy spectrum, and this can have important consequences for the interpretation of geomagnetic observations.

The observed decrease in the toroidal component of the kinetic energy evidently leads to a decrease in the hydrodynamic helicity: from the state without a magnetic field with $\mathcal{H}_a^{\mathcal{H}} = \overline{|\mathbf{V} \cdot \mathrm{curl}\mathbf{V}|} = (7.6 \pm 1.5) \times 10^5$ to $\mathcal{H}_a^{\mathcal{H}} = (5.8 \pm 1.7) \times 10^5$ for $t > t_3$ (Fig. 10). The ratio of helicities during the transition under consideration coincides with the ratio of kinetic energies. In general, the observed decrease in the kinetic energy and hydrodynamic helicity is not the only possible factor suppressing the magnetic field generation. According to the mean field dynamo theory, the generation of the mean magnetic field $\frac{\partial \mathbf{B}}{\partial t} \sim \mathrm{curl}(\alpha\mathbf{B})$ depends precisely on the total α-effect, including the contribution from the magnetic helicity $\mathcal{H}^{\mathcal{M}}$ [Zeldovich et al., 1983; Brandenburg and Subramanian, 2005]:

$$\alpha = \alpha^{\mathcal{H}} + \alpha^{\mathcal{M}}, \quad \alpha^{\mathcal{H}} = \frac{\tau}{3}\mathcal{H}^{\mathcal{H}}, \quad \alpha^{\mathcal{M}} = -\frac{\tau}{3}\mathcal{H}^{\mathcal{M}}; \quad (16)$$

therefore, an additional purely magnetic decrease in α is possible via $\alpha^{\mathcal{M}}$ (here τ is the characteristic time of vortex revolution). On the other hand, the creation of a nonzero field $\mathcal{H}^{\mathcal{M}}$ is impossible due to the law of conservation of magnetic helicity; i.e., $\mathcal{H}^{\mathcal{M}}$ must be scale-partitioned, so that the magnetic helicity will be of one sign on some scales and of the opposite sign on others. Such an analysis is outside the scope of this work.

5. DISCUSSION

The magnetic fields of planets are an extremely important source of information about the processes operating in liquid cores over times of 10^2–10^3 years and more. Some insights into the energy spectra of the magnetic field in upper layers of cores can be gained from the variations in the poloidal component of the field at the surface of the planets, whereas the analysis of the magnetic field energy spectra in the conducting cores themselves, as well as the kinetic energy spectra, remains the subject of theory. Using the dynamo model in a rectangular box introduced in this paper, we examined the characteristic magnetostrophic regimes, some dependences of kinetic energy spectra on the amplitude of thermal sources, and implications of the presence of a magnetic field in the system. It is interesting that, as already noted in [Reshetnyak, 2005], the spectra can be significantly anisotropic; typically, the field spectra in the vertical direction monotonically decrease, while, in the horizontal direction, they have a maximum on the scales of geostrophic columns $\sim 1/k_c$. On the other hand, the α-effect created by these columns generates a magnetic field with a decreasing spectrum. At a certain time moment, the resulting magnetic field reorganizes flows and begins to impede the cyclonic rotation, thereby suppressing the α-effect and stopping a further rise in the magnetic field. This scenario describes real processes only very approximately; this calls for a componentwise analysis of energy fluxes in the system on different scales, and we plan to perform this task in the future.

ACKNOWLEDGMENTS

I am grateful to D.D. Sokolov for discussions. This work was supported by the Russian Foundation for Basic Research, project no. 03-05-64074, and INTAS, grant no. 03-51-5807.

REFERENCES

1. A. Brandenburg and K. Subramanian, "Astrophysical Magnetic Fields and Nonlinear Dynamo Theory," Phys. Rep. **417**, 1–209 (2005).
2. B. Buffett, "A Comparison of Subgrid-Scale Models for Large-Eddy Simulations of Convection in the Earth's Core," Geophys. J. Int. **153**, 753–765 (2003).
3. F. H. Busse, "Thermal Instabilities in Rapidly Rotating Systems," J. Fluid Mech. **44**, 441–460 (1970).
4. C. Canuto, M. Y. Hussaini, A. Quarteroni, and T. A. Zang, *Spectral Methods in Fluids Dynamics* (Springer, New York, 1988).
5. F. Cattaneo, T. Emonet, and N. Weis, "On the Interaction between Convection and Magnetic Fields," ApJ **588**, 1183–1198 (2003).
6. S. Chandrasekhar, *Hydrodynamics and Hydromagnetic Stability* (Dover, New York, 1961).
7. U. Frisch, *Turbulence: The Legacy of A.N. Kolmogorov* (Cambridge Univ. Press, Cambridge, 1995).
8. A. V. Getling, *Rayleigh–Benard Convection: Structures and Dynamics* (Editorial URSS, Moscow, 1999) [in Russian].
9. G. A. Glatzmaier and P. H. Roberts, "A Three-Dimension Self-Consistent Computer Simulation of a Geomagnetic Field Reversal," Nature **377**, 203–209 (1995).
10. R. Hollerbach and R. Rüdiger, *The Magnetic Universe* (Wiley–VCH, Weinheim, 2004).
11. C. A. Jones and P. H. Roberts, "Convection Driven Dynamos in a Rotating Plane Layer," J. Fluid Mech. **404**, 311–343 (2000).

12. C. A. Jones, "Convection-Driven Geodynamo Models," Phil. Trans. R. Soc. **358A**, 873–897 (2000).
13. F. Krause and K.-H. Rädler, *Mean Field Magnetohydrodynamics and Dynamo* (Akademie, Berlin, 1980; Mir, Moscow, 1984).
14. C. Kutzner and U. R. Cristensen, "From Stable Dipolar towards Reversing Numerical Dynamos," Phys. Earth Planet. Inter. **131**, 29–45 (2002).
15. L. D. Landau and E. M. Lifshitz, *Course of Theoretical Physics*, Vol. 8: *Electrodynamics of Continuous Media* (Nauka, Moscow, 1982; Pergamon, New York, 1984).
16. M. Lesieur, *Turbulence in Fluids* (Kluwer, London, 1997).
17. M. Meneguzzi and A. Pouquet, "Turbulent Dynamos Driven by Convection," J. Fluid Mech. **205**, 297–318 (1989).
18. H. K. Moffat, *Magnetic Field Generation in Electrically Conducting Fluids* (Cambridge Univ. Press, Cambridge, 1978; Mir, Moscow, 1980).
19. S. A. Orszag, "Numerical Simulation of Incompressible Flows within Simple Boundaries. I. Galerkin (Spectral) Representations," Stud. Appl. Math. **L** (51), 293–327 (1971).
20. W. H. Press, S. A. Teukolsky, and B. P. Flannery, *Numerical Recipes in Fortran 90. The Art of Parallel Scientific Computing*, 2nd ed., 2 vols. (Cambridge Univ. Press, Cambridge, 2002).
21. M. Yu. Reshetnyak, "Estimation of the Turbulent Viscosity in the Earth's Liquid Core," Dokl. Ross. Akad. Nauk **400** (1), 105–109 (2005).
22. M. Yu. Reshetnyak, "Hydrodynamic Helicity in Boussinesq-Type Models of the Geodynamo," Fiz. Zemli, No. 6, 3–13 (2006) [Izvestiya, Phys. Solid Earth **42**, 449–459 (2006)].
23. M. Reshetnyak and B. Steffen, "Dynamo Model in the Spherical Shell," Numer. Methods and Programming **6**, 27–32 (2005).
24. P. H. Roberts, "On the Thermal Instability of a Highly Rotating Fluid Sphere," Astrophys. J. **141**, 240–250 (1965).
25. A. A. Ruzmaikin, "Origin of Sunspots," Space Sci. Rev. **95**, 43–53 (2001).
26. G. R. Sarson, C. A. Jones, and A. W. Longbottom, "The Influence of the Boundary Region Heterogeneities on the Geodynamo," Phys. Earth Planet. Inter. **101**, 13–32 (1997).
27. H. Schlichting, *Boundary Layer Theory*, 6th ed. (McGraw-Hill, New York, 1968; Nauka, Moscow, 1974].
28. R. Ph. D. Simitev, Convection and Magnetic Field Generation in Rotating Spherical Fluid Shells, *Thesis of Dissertation*, Bayreuth: Univ. of Bayreuth, 2004, p. 193 (http://www.phy.uni-bayreuth.de/theo/tp4/members/simitev.html).
29. P. Tabeling, "Two-Dimensional Turbulence: A Physicist Approach," Phys. Rep. **362**, 1–62 (2002).
30. Ya. B. Zeldovich, A. A. Ruzmaikin, and D. D. Sokoloff, *Magnetic Fields in Astrophysics* (Gordon and Breach, New York, 1983).